Gate-tunable h/e-period magnetoresistance oscillations in Bi_2O_2Se nanowires

Jianghua Ying,[1,2] Guang Yang,[1,2] Zhaozheng Lyu,[1,2] Guangtong Liu,[1] Zhongqing Ji,[1] Jie Fan,[1] Changli Yang,[1] Xiunian Jing,[1] Huaixin Yang,[1,2] Li Lu,[1,2,3,4,*] and Fanming Qu[1,3,4,*]

[1]*Beijing National Laboratory for Condensed Matter Physics, Institute of Physics, Chinese Academy of Sciences, Beijing 100190, China*

[2]*School of Physical Sciences, University of Chinese Academy of Sciences, Beijing 100049, China*

[3]*CAS Center for Excellence in Topological Quantum Computation, University of Chinese Academy of Sciences, Beijing 100190, China*

[4]*Songshan Lake Materials Laboratory, Dongguan, Guangdong 523808, China*

(Received 23 May 2019; revised manuscript received 10 November 2019; published 18 December 2019)

We report on the successful synthesis and low-temperature electron transport investigations of a new form of material—Bi_2O_2Se semiconducting nanowires. Gate-tunable 0- and π-h/e (h is the Planck constant and e the elementary charge) periodic resistance oscillations in longitudinal magnetic field were observed unexpectedly, demonstrating novel quasiballistic, phase-coherent surface states in Bi_2O_2Se nanowires. By reaching a very good agreement between the calculated density of states and the experimental data, we clarified the mechanism to be the one-dimensional subbands formed along the circumference of the nanowire rather than the usually considered Aharonov-Bohm interference. A qualitative physical picture based on downward band bending associated with the complex band structure is proposed to describe the formation of the surface states.

DOI: 10.1103/PhysRevB.100.235307

I. INTRODUCTION

New-type low-dimensional materials have attracted tremendous interest due to their intriguing properties and application potentials in next-generation electronics, optoelectronics, etc. Graphene, phosphorene, and transition-metal dichalcogenide are among the star materials [1–3]. However, drawbacks also exist in these materials, either lack of a bandgap, instable in air, or with only a moderate electron mobility. Recently, a new layered semiconductor Bi_2O_2Se has drawn ever-growing attention due to its superior electronic properties such as an ultrahigh electron mobility ($\sim 2.8 \times 10^5\,cm^2/V\,s$ at 2 K), a tunable bandgap ($\sim$0.8 eV), and being stable in ambient environment [4–21]. Large-scale Bi_2O_2Se thin films from monolayer to few layer have been successfully synthesized through a chemical vapor deposition method [4,17]. The existence of strong spin-orbit interaction [21] and high-performance field-effect transistors and optoelectronics [4,11,12,15,19,22] have also been experimentally demonstrated. And the ferroelectricity/ferroelasticity is further expected [8].

Given the fascinating features in the two-dimensional (2D) form of Bi_2O_2Se, it is natural to expect that the one-dimensional (1D) nanowire form of Bi_2O_2Se, with large surface-to-volume ratio, would retain some of the unique properties of its 2D counterpart. However, investigation of Bi_2O_2Se nanowires is still a mysterious veil at present. In this work, we report on the synthesis of high-quality single-crystalline Bi_2O_2Se nanowires by means of a gold-catalyzed vapor-liquid-solid (VLS) mechanism. Low-temperature electron transport measurements reveal h/e-period resistance oscillations as a function of longitudinal magnetic field (h is the Planck constant and e the elementary charge) and a gate-tunable π-phase shift. These unexpected observations demonstrate quasiballistic, phase-coherent electron transport of surface states in Bi_2O_2Se nanowires. A very good agreement between the calculated density of states and the experimental results—the double modulation of the resistance oscillations by gate voltage and magnetic field—clarifies the mechanism to be the 1D subbands formed along the circumference of the nanowire rather than the usually considered Aharonov-Bohm interference. A qualitative picture associated with the complex band structure is further proposed to interpret the formation of surface electron accumulation based on downward band bending.

II. CHARACTERIZATION

Bi_2O_2Se nanowires were synthesized via a gold-catalyzed VLS mechanism on Si wafers in a horizontal tube furnace with Bi_2Se_3 powder as the source material. A detailed phase equilibrium process can be found in the Supplemental Material [23]. After growth, the wafer appeared to be gray as an evidence of nanowire production. Figure 1(a) shows the scanning electron microscopy (SEM) image of the as-synthesized Bi_2O_2Se nanowires, which have a length of 5–10 μm and a diameter of 80–250 nm.

To characterize the basic crystal structure, we have carried out an extensive transmission electron microscopy (TEM) study on the as-synthesized samples. Figure 1(b) shows a bright-field TEM image and the corresponding diffraction pattern taken along the [010] zone axis direction of one typical nanowire. All the main diffraction spots in these patterns can be well indexed using the expected tetragonal unit cell with lattice parameters of about $a = 0.389$ nm, $c = 1.22$ nm (space group $I4/mmm$) [4], which agree well with the x-ray powder diffraction result as shown in the Supplemental Material [23]. A better and very clear view of the atomic structure for

*Corresponding authors: lilu@iphy.ac.cn; fanmingqu@iphy.ac.cn

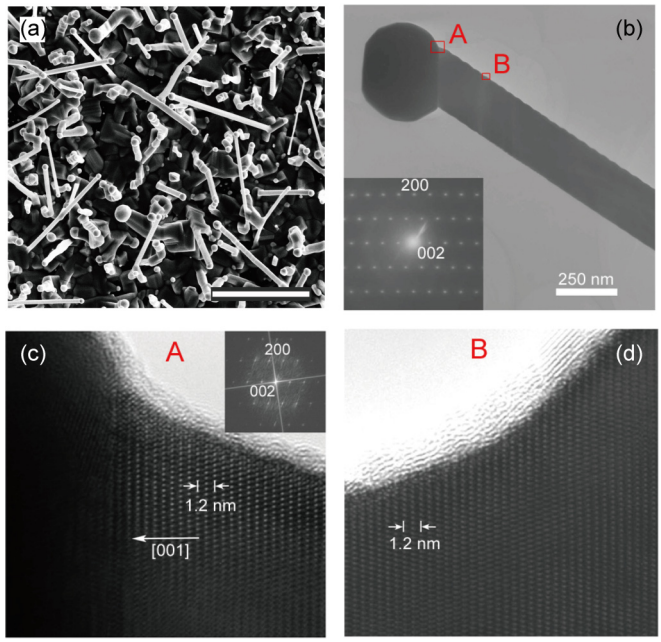

FIG. 1. (a) SEM image of the as-synthesized Bi_2O_2Se nanowires on Si wafer. Scale bar 5 μm. The ball on the top of the nanowire is the Au catalyst. (b) A bright-field TEM image and the corresponding diffraction pattern taken along the [010] zone axis direction of one typical nanowire. (c), (d) The HRTEM images taken from the square-enclosed A and B regions in (b), respectively. The inset in (c) presents the FFT spectrum.

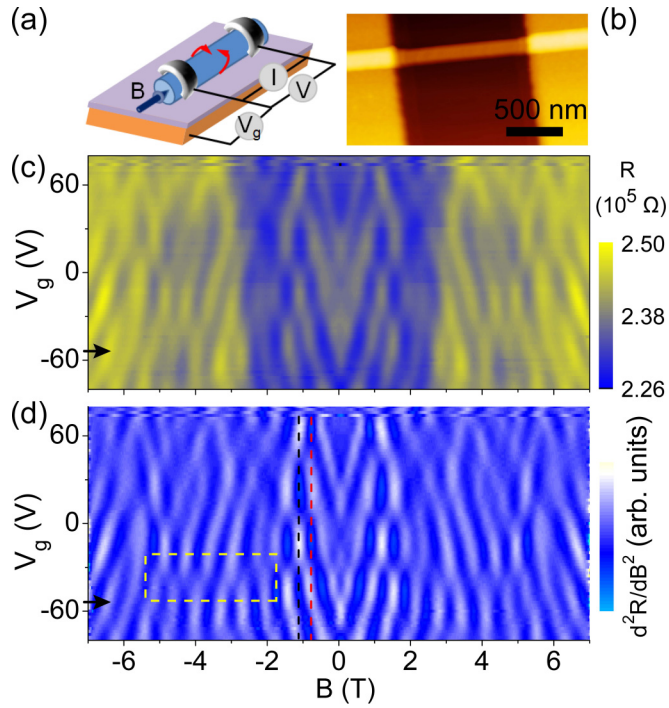

FIG. 2. (a) Sketch of two-terminal measurement configuration. A longitudinal magnetic field B and a back-gate voltage V_g are applied. (b) Atomic force microscopy (AFM) image of device No. 1 with two Ti/Au contacts. (c) Color map of the two-terminal resistance R vs B and V_g at 1.8 K. (d) Second-order derivatives of the smoothed data from (c), clearly illustrating the oscillations. The yellow rectangle region highlights the π-phase shifts. The black and red dashed lines mark the two line cuts in Fig. 3(e). The arrows in (c) and (d) indicate the positions of the line cuts in Figs. 3(a) and 3(c), respectively.

the various positions has been obtained by high-resolution TEM (HRTEM) observations. Figures 1(c) and 1(d) show the HRTEM images taken from the square-enclosed A and B regions in Fig. 1(b), respectively. It can be seen from Fig. 1(b) that the Bi_2O_2Se nanowire attaches with one well-defined facet of gold nanoparticle and grows along the [001] direction. From Fig. 1(b) we can conclude that there is an angle between the [001] atomic layer and the growth direction (the long axis direction) of the nanowire.

The HRTEM images in Fig. 1(b) also indicate the presence of a zigzag structure along the edge of the as-prepared nanowires. Figure 1(d) illustrates the HRTEM image taken from region B, demonstrating that there is no obvious planar defect in such areas. The layered structural morphologies are very likely caused by a layer-by-layer growth mode, in which there could be a relative shift in the *ab* plane during the crystal growth due to the specific synthesis condition. These spectroscopic characterizations demonstrate that the as-synthesized Bi_2O_2Se nanowires are of high quality.

III. GATE TUNABLE OSCILLATIONS

For electron transport measurements, Bi_2O_2Se nanowires were mechanically transferred onto a highly doped Si substrate with a 300-nm-thick SiO_2 layer used for applying a back-gate voltage. Ti/Au (5 nm/150 nm) contacts were deposited using a standard lithography technique. Two-terminal measurements were carried out with a temperature down to 1.8 K and a magnetic field up to 7 T.

Figure 2(a) shows a sketch of the measurement setup. The large surface-to-volume ratio of the nanowire provides excellent geometries for probing the transport properties of surface states, if present, as indicated by the red arrows in Fig. 2(a). Figure 2(b) presents an atomic force microscopy (AFM) image of device No. 1 with two bright Ti/Au contacts. Figure 2(c) displays the two-terminal resistance versus magnetic field B applied along the axis of the nanowire and back-gate voltage V_g at 1.8 K for device No. 1. In order to identify the oscillating features more clearly, we smoothed the data of Fig. 2(c) and extracted the second-order derivatives, i.e., the phase diagram, as shown in Fig. 2(d).

One obvious characteristic of Figs. 2(c) and 2(d) is that the resistance oscillates as a function of B. The periodic oscillations in magnetic field along the nanowire axis [see representative curves in Figs. 3(a) and 3(c)] indicate a well-defined surface-conducting channel to pick up flux [24]. Such periodic oscillations with a period of h/e or $h/2e$ have been observed in many 1D systems with a surface-conducting layer [24], such as metallic cylinders [25], carbon nanotubes [26], core/shell nanowires [27,28], semiconducting nanowires [29], topological insulator nanoribbons [30,31], Dirac semimetal nanowires [32], etc. Note that only a few small-band-gap semiconductors carry intrinsic electron-accumulated surface states, such as InN, InAs, and ZnO [33–35]. In addition, per-

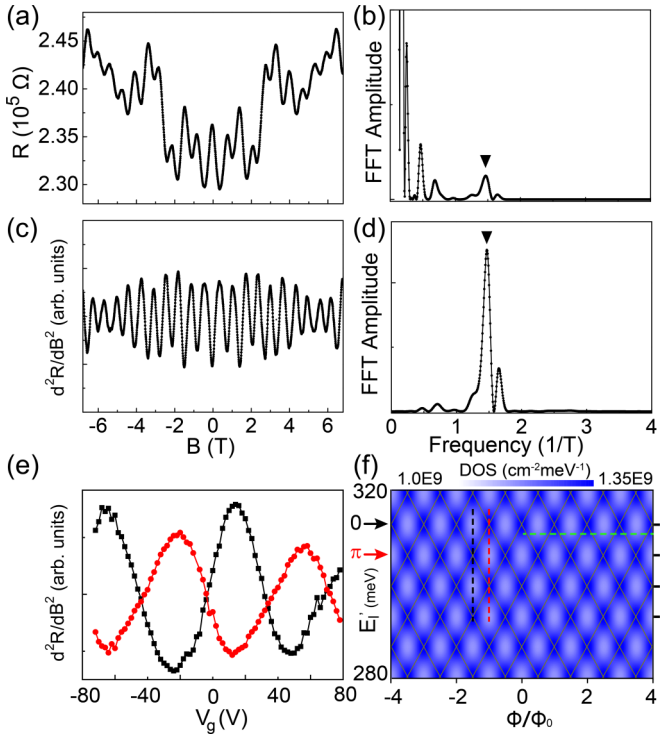

FIG. 3. (a) R vs B curve at $V_g = -54$ V taken out from Fig. 2(c). (b) FFT of R vs B curve in (a). (c) Second-order derivative d^2R/dB^2 of the smoothed R vs B curve in (a) and its FFT pattern is shown in (d). The triangles in (b) and (d) denote the main peak at $1.46\,\mathrm{T}^{-1}$. (e) Two line cuts of d^2R/dB^2 vs V_g taken out from Fig. 2(d) as marked by the black ($B = -1.13$ T) and red ($B = -0.73$ T) dashed lines, respectively. (f) Subbands formed at the circumference of the nanowire as a function of longitudinal magnetic flux Φ, without level broadening (solid gray lines) and with level broadening (DOS represented by bluish background colors). The green dashed line indicates Φ_0-period (irregular) oscillations with (without) level broadening, while the bars show Φ_0-period oscillations for both cases. A π-phase shift exists both in the V_g dependence of oscillations (i.e., along the dashed black and red line cuts) and in the Φ dependence of oscillations (i.e., line cuts along the black and red arrows).

sistent currents in normal-metal rings parallels with equivalent results [36–38].

In a mesoscopic ring, the mechanism of periodic resistance oscillations is relatively straightforward. The $h/2e$-period oscillations, named Altshuler-Aronov-Spivak oscillations [39], result from the interference of partial waves between a pair of time-reversed paths, sharing the same mechanism as weak localization. On the other hand, the h/e-period oscillations are associated with the interference of partial waves through two different possible paths from one terminal to the other one, called Aharonov-Bohm (AB) oscillations [40].

For cylindrical shell conductors, $h/2e$ oscillations are usually observed at low magnetic fields and die out and disappear at high magnetic fields due to the requirement of time-reversal symmetry [41]. On the contrary, the h/e oscillations can survive at both high and low magnetic fields, without the need of time-reversal symmetry. The periodic oscillations in Figs. 2(c) and 2(d) survive at high magnetic fields (± 7 T), and thus they are consistent with h/e oscillations. However, the h/e oscillations require ballistic transport [28,29]. In such cases, although it is still called AB oscillation [40], the underlying mechanism transits to the modulation of density of states by magnetic field rather than AB interference. The ballistic transport of electrons along the circumference forms 1D subbands with different angular momentum which is regulated by the penetrated magnetic field [28,29,42,43], as explained later. The competition between the h/e and $h/2e$ components depends on the strength of the disorder and the size of the cylinder [29,32,44].

To analyze the oscillations as a function of longitudinal magnetic field, we take typical line cuts at $V_g = -54$ V from Figs. 2(c) and 2(d) (marked by the black arrows), as shown in Figs. 3(a) and 3(c), respectively. The periodic oscillations can be clearly recognized. Figure 3(b) shows the fast Fourier transform (FFT) spectrum of the R vs B curve in Fig. 3(a). A prominent peak can be found at a frequency of $f = 1.46\,\mathrm{T}^{-1}$ as depicted by the triangle. The low-frequency peaks correspond to the large-scale background variation of Fig. 3(a), presumably due to universal conductance fluctuations (UCFs) of the bulk states. These false peaks can be readily suppressed by taking the FFT spectrum of the second-order derivative d^2R/dB^2, a method commonly applied to separate the oscillatory part from background, as shown in Fig. 3(d). The h/e-periodic oscillations are thus associated with an area of $S = f \times h/e = 6050\,\mathrm{nm}^2$, where S is the cross-section area of the nanowire. Taking the nearly elliptical cross-section dimensions, a width of 140 nm and a height of 95 nm, we need to assume a depth d of the surface states [30] to match the required area. $d \sim 6$ nm was deduced from $\pi \times (65\text{-}d) \times (42.5\text{-}d) = S$ after subtracting the surface undulation of 5 nm due to zigzag structures. Note that the dimensions might be overestimated from SEM or AFM images. Nevertheless, the $h/2e$ oscillations at a double frequency $2f$ were invisible. Combining the dominant h/e oscillations and the superposition of UCFs, we conclude that our Bi_2O_2Se nanowires are in the quasiballistic regime [27,29,45].

Another noticeable characteristic of Figs. 2(c) and 2(d) is that the resistance changes between a peak and a valley alternatively along gate voltage (even without magnetic field). Figure 3(e) depicts two curves of d^2R/dB^2 vs V_g taken out from Fig. 2(d) at $B = -1.13$ T and -0.73 T, as marked by the black and red dashed lines, respectively. The oscillating behavior arises from the variation of the density of states as tuning the Fermi level by V_g (as explained later). The opposite phase of these two oscillating curves demonstrates a relative π-phase shift. Under the double modulation by V_g and B, the π-phase shift along V_g also represents tuning between the 0- and π-h/e oscillations along B, i.e., starting from low and high resistance at zero magnetic field, respectively. Such π-phase shift along B is more obvious in the dashed rectangle in Fig. 2(d).

IV. THEORETICAL FRAMEWORK

In the following we explain the above observations consistently within the theoretical framework of ballistic electron transport through cylindrical surface states penetrated by a magnetic flux [28,29,32,46]. The motion of surface electrons along the cylindrical shell can be regarded as a combination

of a circular component and a free component along the nanowire axis z. The Hamiltonian can be written as

$$\hat{H}=\frac{1}{2m^*r_0^2}\left(L_z-\frac{1}{2}eB_zr_0^2\right)^2-\frac{\hbar^2}{2m^*}\frac{\partial^2}{\partial z^2},$$

where L_z denotes the angular momentum operator and r_0 the radius of the nanowire. With $\pi {r_0}^2 B_z = \Phi$ as the magnetic flux through the circular loop and $\Phi_0 = h/e$, we find the energy eigenvalues as

$$E_l = \frac{\hbar^2 k_z^2}{2m^*}+\frac{\hbar^2}{2m^*{r_0}^2}\left(l-\frac{\Phi}{\Phi_0}\right)^2.$$

The first term describes the kinetic energy for the motion along z. The second term, where the angular momentum quantum number $l = 0, \pm1, \pm2\ldots$, represents a series of parabolas as a function of Φ shifted to each other by Φ_0. The energetic spectrum for $k_z = 0$ ($E_l{}'$) with each parabola belonging to a specific angular momentum state is illustrated in Fig. 3(f) by the solid gray lines. However, in contrast to the experimental observations shown in Figs. 2(c) and 2(d), h/e-periodic oscillations along B are only expected at certain discrete energies, as marked by the black bars on the right in Fig. 3(f). And irregular oscillations dominate for most of the energies, as represented by the horizontal green dashed line in Fig. 3(f). We argue that level broadening of the subbands presumably arising from thermal broadening, inelastic scattering, and/or finite thickness of the surface channel (uncertainty of flux) should be taken into account.

From the red line of Fig. 3(e), we take one full oscillation from $V_g = -64$ V to 12 V to estimate the Fermi-level position. Under the assumption of finite bulk contributions, this gate-voltage range corresponds to a Fermi level shift of 13.2 meV (subband separation) [23]. Using $E_l{}'(\Phi = 0) = \frac{\hbar^2}{2m^*r_0^2}l^2$, we extract the Fermi level at $V_g = -64$ V to be 299.4 meV ($l = \pm46$), and at $V_g = 12$ V to be 312.6 meV ($l = \pm47$). The colored background of Fig. 3(f) depicts the calculated density of states (DOS) by approximating level broadening as a Lorentz shape distribution. Clearly, the double modulation by B and V_g gives rise to the Φ_0-period DOS (resistance) oscillations along B as well as the π-phase shift. When V_g tunes the Fermi level, the DOS (resistance) also oscillates at a given B. The opposite phase between the black and red dashed lines can be apparently recognized, as shown by the two experimental curves in Fig. 3(e) accordingly. The π-phase shift, i.e., the 0- and π-h/e oscillations, as marked by the black (DOS peak at $\Phi = 0$) and red (DOS valley at $\Phi = 0$) arrows in Fig. 3(f), respectively, can be immediately identified. Note that the DOS map in Fig. 3(f) represents a qualitative interpretation of the data. Details of the extraction of the DOS color map can be found in the Supplemental Material [23].

Furthermore, we have performed systematic measurements of gate-dependent h/e oscillations on device No. 2. Consistent oscillations as a function of both B and V_g were observed, as shown in Figs. 4(a) and 4(b), including the alternation between resistance peaks and valleys at $B = 0$ and the π-phase shift [marked by the dashed line in Fig. 4(b)].

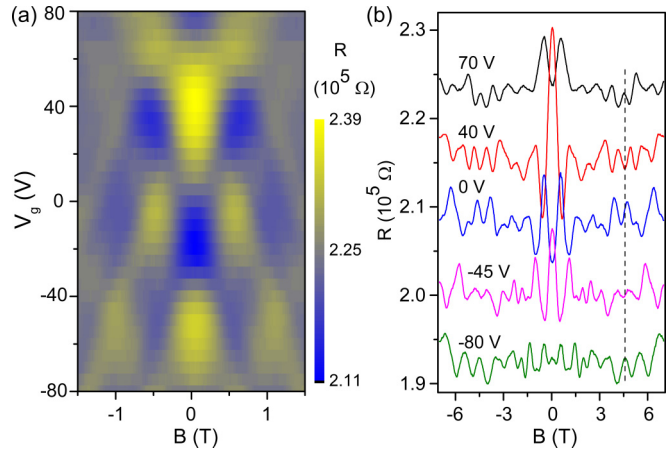

FIG. 4. (a) Resistance R of device No. 2 as a function of both B and V_g at 1.8 K. (b) R vs B curves at different V_g with an offset for clarity. The black dashed line guides the π-phase shift between different curves.

V. DISCUSSION

Next we propose a qualitative physical picture to describe the formation of surface-conducting channels on Bi_2O_2Se. For semiconductors, the surface Fermi level E_F tends to sit at a universal value of ~4.9 eV [47] or ~4.5 eV (with hydrogen adsorbed) [33] below the vacuum level to reach charge neutrality. This charge neutrality level, called branch point energy (E_B), represents the separation of donor-type (below) and acceptor-type (above) states at the surface/interface [48]. It also corresponds to the average midgap energy weighting the entire Brillouin zone in the complex band structures [49]. For a few small-band-gap semiconductors with an extremely low conduction-band minimum (E_C) and a small effective mass, the density of states around the Γ point is negligible compared to other band edges at the boundaries of the Brillouin zone. Therefore, the average midgap energy E_B could be higher than E_C, such as in InN, InAs, and ZnO [33–35]. The direct result is the existence of donor-type states at the surface and thus the downward band bending and accumulation of electrons near the surface.

Regarding Bi_2O_2Se, the band structures indeed show a low E_C at Γ point, ~0.8 eV above the valence band maximum E_V, with a relative small effective mass of $0.14m_0$ (m_0 is the free electron mass) [4]. Consequently, it is possible that E_B is higher than E_C. Applying similar approximations as for small gap III-V semiconductors [49], the midgap energy at the X point, the zone face center, indeed crosses the conduction band at the Γ point [4,7,8,10,50]. Due to the variation between the band structures of Bi_2O_2Se obtained by different methods [4,7,8,10,15,50–52], however, we seek to propose a possible qualitative picture in the current work. Assuming that E_B is higher than E_C and a position of E_F in the gap, the band alignment near the surface is illustrated in Fig. 5. The unoccupied donor-type states at the surface are positively charged, balanced by the downward band-bending-induced space charge. Near the surface, E_F crosses E_C, and thus electrons accumulate to form surface-conducting channels. Note that this mechanism originates from the intrinsic

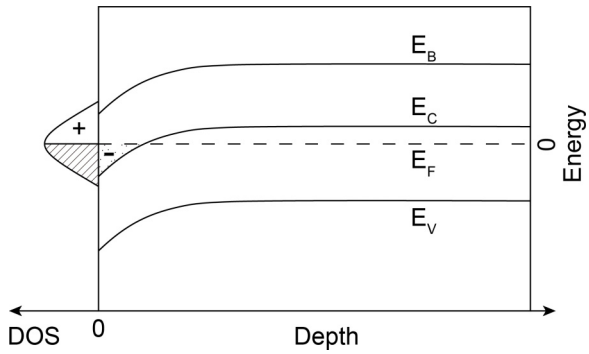

FIG. 5. The branch point energy E_B is assumed to be higher than the conduction-band minimum E_C. The left side of the figure shows the density of states of the donor-type states at the surface, which are positively charged when unoccupied. The band bends downward to reach charge neutrality, resulting in the crossing of Fermi level E_F with conduction band and thus electron accumulation near the surface.

donor-type states at the surface. Further detailed investigations are required to shed more light on the surface states of Bi_2O_2Se.

VI. SUMMARY

In summary, we synthesized high-quality Bi_2O_2Se nanowires by means of a gold-catalyzed VLS method. The single-crystalline nature of Bi_2O_2Se nanowire as a typical bismuth-based oxychalcogenide material was confirmed by x-ray diffraction and transmission electron microscopy. The gate-tunable h/e-period oscillations were observed and attributed to the quasiballistic transport through the surface states of Bi_2O_2Se nanowires. These results clearly demonstrate a new type of semiconducting nanowire with quasi-1D electron subbands of different angular momentum at the surface, which provides an ideal platform for the design of future quantum electronics. A possible intrinsic mechanism is proposed for the formation of electron accumulation, which, however, deserves further detailed theoretical and experimental inspection.

ACKNOWLEDGMENTS

We would like to thank Yugui Yao, Xuefeng Wang, Fan Yang, Jun Chen, and Yongqing Li for fruitful discussions. This work was supported by the National Basic Research Program of China through MOST Grants No. 2017YFA0304700, No. 2016YFA0300601, and No. 2015CB921402; by the NSF China through Grants No. 11527806, No. 91221203, No. 11174357, No. 91421303, and No. 11774405; by the Open Research Fund from the State Key Laboratory of High Performance Computing of China; by the Beijing Academy of Quantum Information Sciences, Grant No. Y18G08; and by the Strategic Priority Research Program B of Chinese Academy of Sciences, Grants No. XDB28000000 and No. XDB07010100.

[1] K. S. Novoselov, A. K. Geim, S. V. Morozov, D. Jiang, Y. Zhang, S. V. Dubonos, I. V. Grigorieva, and A. A. Firsov, Science **306**, 666 (2004).
[2] B. Radisavljevic, A. Radenovic, J. Brivio, V. Giacometti, and A. Kis, Nat. Nanotechnol. **6**, 147 (2011).
[3] L. Li, Y. Yu, G. J. Ye, Q. Ge, X. Ou, H. Wu, D. Feng, X. H. Chen, and Y. Zhang, Nat. Nanotechnol. **9**, 372 (2014).
[4] J. Wu, H. Yuan, M. Meng, C. Chen, Y. Sun, Z. Chen, W. Dang, C. Tan, Y. Liu, J. Yin, Y. Zhou, S. Huang, H. Q. Xu, Y. Cui, H. Y. Hwang, Z. Liu, Y. Chen, B. Yan, and H. Peng, Nat. Nanotechnol. **12**, 530 (2017).
[5] J. Wu, C. Tan, Z. Tan, Y. Liu, J. Yin, W. Dang, M. Wang, and H. Peng, Nano Lett. **17**, 3021 (2017).
[6] J. Wu, Y. Liu, Z. Tan, C. Tan, J. Yin, T. Li, T. Tu, and H. Peng, Adv. Mater. **29**, 1704060 (2017).
[7] H. Fu, J. Wu, H. Peng, and B. Yan, Phys. Rev. B **97**, 241203 (2018).
[8] M. Wu and X. C. Zeng, Nano Lett. **17**, 6309 (2017).
[9] U. Khan, Y. Luo, L. Tang, C. Teng, J. Liu, B. Liu, and H.-M. Cheng, Adv. Funct. Mater. **29**, 1807979 (2018).
[10] H. Li, X. Xu, Y. Zhang, R. Gillen, L. Shi, and J. Robertson, Sci. Rep. **8**, 10920 (2018).
[11] J. Li, Z. Wang, Y. Wen, J. Chu, L. Yin, R. Cheng, L. Lei, P. He, C. Jiang, L. Feng, and J. He, Adv. Funct. Mater. **28**, 1706437 (2018).
[12] X. Tian, H. Luo, R. Wei, C. Zhu, Q. Guo, D. Yang, F. Wang, J. Li, and J. Qiu, Adv. Mater. **30**, 1801021 (2018).
[13] T. Tong, M. Zhang, Y. Chen, Y. Li, L. Chen, J. Zhang, F. Song, X. Wang, W. Zou, Y. Xu, and R. Zhang, Appl. Phys. Lett. **113**, 072106 (2018).
[14] C. Zhu, T. Tong, Y. Liu, Y. Meng, Z. Nie, X. Wang, Y. Xu, Y. Shi, R. Zhang, and F. Wang, Appl. Phys. Lett. **113**, 061104 (2018).
[15] Q. Fu, C. Zhu, X. Zhao, X. Wang, A. Chaturvedi, C. Zhu, X. Wang, Q. Zeng, J. Zhou, F. Liu, B. K. Tay, H. Zhang, S. J. Pennycook, and Z. Liu, Adv. Mater. **31**, 1804945 (2019).
[16] C. Tan, M. Tang, J. Wu, Y. Liu, T. Li, Y. Liang, B. Deng, Z. Tan, T. Tu, Y. Zhang, C. Liu, J.-H. Chen, Y. Wang, and H. Peng, Nano Lett. **19**, 2148 (2019).
[17] J. Wu, C. Qiu, H. Fu, S. Chen, C. Zhang, Z. Dou, C. Tan, T. Tu, T. Li, Y. Zhang, Z. Zhang, L.-M. Peng, P. Gao, B. Yan, and H. Peng, Nano Lett. **19**, 197 (2019).
[18] Z. Zhang, T. Li, Y. Wu, Y. Jia, C. Tan, X. Xu, G. Wang, J. Lv, W. Zhang, Y. He, J. Pei, C. Ma, G. Li, H. Xu, L. Shi, H. Peng, and H. Li, Adv. Mater. **31**, 1805769 (2019).
[19] J. Yang, R. Quhe, Q. Li, S. Liu, L. Xu, Y. Pan, H. Zhang, X. Zhang, J. Li, J. Yan, B. Shi, H. Pang, L. Xu, Z. Zhang, J. Lu, and J. Yang, Adv. Electron. Mater. **5**, 1800720 (2019).
[20] C. Chen, M. Wang, J. Wu, H. Fu, H. Yang, Z. Tian, T. Tu, H. Peng, Y. Sun, X. Xu, J. Jiang, N. B. M. Schröter, Y. Li, D. Pei, S. Liu, S. A. Ekahana, H. Yuan, J. Xue, G. Li, J. Jia, Z. Liu, B. Yan, H. Peng, and Y. Chen, Sci. Adv. **4**, eaat8355 (2018).

[21] M. Meng, S. Huang, C. Tan, J. Wu, Y. Jing, H. Peng, and H. Q. Xu, Nanoscale **10**, 2704 (2018).
[22] R. Quhe, J. Liu, J. Wu, J. Yang, Y. Wang, Q. Li, T. Li, Y. Guo, J. Yang, H. Peng, M. Lei, and J. Lu, Nanoscale **11**, 532 (2019).
[23] See Supplemental Material at http://link.aps.org/supplemental/10.1103/PhysRevB.100.235307 for additional figures and analysis.
[24] A. G. Aronov and Y. V. Sharvin, Rev. Mod. Phys. **59**, 755 (1987).
[25] D. Y. Sharvin and Y. V. Sharvin, JETP Lett. **34**, 272 (1981).
[26] A. Bachtold, C. Strunk, J.-P. Salvetat, J.-M. Bonard, L. Forró, T. Nussbaumer, and C. Schönenberger, Nature (London) **397**, 673 (1999).
[27] M. Jung, J. S. Lee, W. Song, Y. H. Kim, S. D. Lee, N. Kim, J. Park, M.-S. Choi, S. Katsumoto, H. Lee, and J. Kim, Nano Lett. **8**, 3189 (2008).
[28] Ö. Gül, N. Demarina, C. Blömers, T. Rieger, H. Lüth, M. I. Lepsa, D. Grützmacher, and T. Schäpers, Phys. Rev. B **89**, 045417 (2014).
[29] T. Richter, C. Blömers, H. Lüth, R. Calarco, M. Indlekofer, M. Marso, and T. Schäpers, Nano Lett. **8**, 2834 (2008).
[30] H. Peng, K. Lai, D. Kong, S. Meister, Y. Chen, X.-L. Qi, S.-C. Zhang, Z.-X. Shen, and Y. Cui, Nat. Mater. **9**, 225 (2009).
[31] L. A. Jauregui, M. T. Pettes, L. P. Rokhinson, L. Shi, and Y. P. Chen, Nat. Nanotechnol. **11**, 345 (2016).
[32] L.-X. Wang, C.-Z. Li, D.-P. Yu, and Z.-M. Liao, Nat. Commun. **7**, 10769 (2016).
[33] C. G. Van de Walle and J. Neugebauer, Nature (London) **423**, 626 (2003).
[34] I. Mahboob, T. D. Veal, C. F. McConville, H. Lu, and W. J. Schaff, Phys. Rev. Lett. **92**, 036804 (2004).
[35] M. Noguchi, K. Hirakawa, and T. Ikoma, Phys. Rev. Lett. **66**, 2243 (1991).
[36] R. Landauer and M. Büttiker, Phys. Rev. Lett. **54**, 2049 (1985).
[37] M. Büttiker, Y. Imry, and R. Landauer, Phys. Lett. A **96**, 365 (1983).
[38] H. Bluhm, N. C. Koshnick, J. A. Bert, M. E. Huber, and K. A. Moler, Phys. Rev. Lett. **102**, 136802 (2009).
[39] B. L. Altshuler, A. G. Aronov, and B. Z. Spivak, Pis'ma Zh. Eksp. Teor. Fiz. **33**, 101 (1981) [JETP Lett. **33**, 94 (1981)].
[40] Y. Aharonov and D. Bohm, Phys. Rev. **115**, 485 (1959).
[41] B. Pannetier, J. Chaussy, R. Rammal, and P. Gandit, Phys. Rev. B **31**, 3209 (1985).
[42] A. Fuhrer, S. Lüscher, T. Ihn, T. Heinzel, K. Ensslin, W. Wegscheider, and M. Bichler, Nature (London) **413**, 822 (2001).
[43] A. Lorke, R. Johannes Luyken, A. O. Govorov, J. P. Kotthaus, J. M. Garcia, and P. M. Petroff, Phys. Rev. Lett. **84**, 2223 (2000).
[44] H. Lüth, C. Blömers, T. Richter, J. Wensorra, S. Estevez Hernandez, G. Petersen, M. Lepsa, T. Schäpers, M. Marso, M. Indlekofer, R. Calarco, N. Demarina, and D. Grützmacher, Phys. Status Solidi C **7**, 386 (2010).
[45] S. Cho, B. Dellabetta, R. Zhong, J. Schneeloch, T. Liu, G. Gu, M. J. Gilbert, and N. Mason, Nat. Commun. **6**, 7634 (2015).
[46] B.-C. Lin, S. Wang, L.-X. Wang, C.-Z. Li, J.-G. Li, D. Yu, and Z.-M. Liao, Phys. Rev. B **95**, 235436 (2017).
[47] J. Wu and W. Walukiewicz, Superlattices Microstruct. **34**, 63 (2003).
[48] H. Lüth, *Solid Surfaces, Interfaces and Thin Films* (Springer-Verlag, Berlin, 2010).
[49] J. Tersoff, Phys. Rev. B **32**, 6968 (1985).
[50] T. Cheng, C. Tan, S. Zhang, T. Tu, H. Peng, and Z. Liu, J. Phys. Chem. C **122**, 19970 (2018).
[51] L. Xu, S. Liu, J. Yang, B. Shi, Y. Pan, X. Zhang, H. Li, J. Yan, J. Li, L. Xu, J. Yang, and J. Lu, J. Phys. Chem. C **123**, 8923 (2019).
[52] Y. Wang, B. Xu, G. Yu, J. Zhang, S. Ma, S. Yuan, T. Sun, and Y. Wang, Japan J. Appl. Phys. **58**, 015501 (2018).